Hierarchical wrinkling patterns†

Hugues Vandeparre,‡[a] Sylvain Gabriele,‡[a] Fabian Brau,[a] Cyprien Gay,[b] Kevin Kit Parker[c] and Pascal Damman*[a]

Received 18th May 2010, Accepted 2nd July 2010
DOI: 10.1039/c0sm00394h

This paper reports a simple and flexible method for generating hierarchical patterns from wrinkling instability. Complex features with gradually changing topographies are generated by using the spontaneous wrinkling of a rigid membrane (titanium) on a soft foundation (polystyrene) compressed *via* the diffusion of a solvent. We show that the morphology of these unreported wrinkled patterns is directly related to the rheological properties of the polymer layer and the geometry of the diffusion front. Based on these ingredients, we rationalize the mechanism for the formation of hierarchical wrinkling patterns and quantify our experimental findings with a simple scaling theory. Finally, we illustrate the relevance of our structuration method by studying the mechanosensitivity of fibroblasts.

Introduction

Structured surfaces are especially attractive in various applications including stretchable electronics,[1] photonics,[2–4] wettability,[5] tissue engineering, implants, cell-based biosensors, high-throughput microarrays, basic cell biology and regenerative biology.[6,7] Various techniques have been employed for the fabrication of micro- and nano-structures on solid substrates, such as colloidal lithography,[8] polymer demixing,[9] electrospinning,[10] nanoimprinting [11] or dip-pen lithography.[12] However these methods have severe drawbacks, including high cost, the substantial inconvenience of using clean room facilities and their inability to generate complex patterns with gradients of amplitudes and tailor-made geometries.

To address the need for a simple, more scalable and cost-effective technique for fabricating micro- and nano-structures, non-lithographic based strategies have been developed based on the wrinkling instability of a compressed rigid membrane on a soft elastic foundation.[13,14] The characteristic dimensions of the uniform wrinkled pattern obtained (*i.e.* amplitude and wavelength) can be easily tuned by setting experimental parameters such as: membrane and film thicknesses, elastic moduli and the applied compressive stress.[13–15] Beside the linear and labyrinthine patterns generally obtained by applying either uniaxial or isotropic stress, a few studies have explored the feasibility to achieve more complex patterns.[13,15–21] These strategies are however all based on edge effects and are thus not suitable to organize the wrinkles on large areas. Recently, we described a new method to generate custom-tailored wrinkled patterns based on the molecular diffusion of solvent through the polymer layer.

Here we propose, by changing the rheological behavior of the polymer layer in which the solvent diffuses, to generate complex hierarchical wrinkled patterns, with a topographical gradient ranging from the nano- to the microscale. We study in detail the mechanism at the origin of these hierarchical wrinkled patterns and finally propose to illustrate the relevance of these complex features by observing cell mechanosensitivity.

Results and discussion

Wrinkling by solvent diffusion

Previous studies showed that metal/polymer/substrate trilayers undergo wrinkling after either an appropriate thermal treatment or the diffusion of a solvent in the polymer layer.[13,15,22,23] As shown in Fig. 1, wrinkling can indeed be induced by immersing

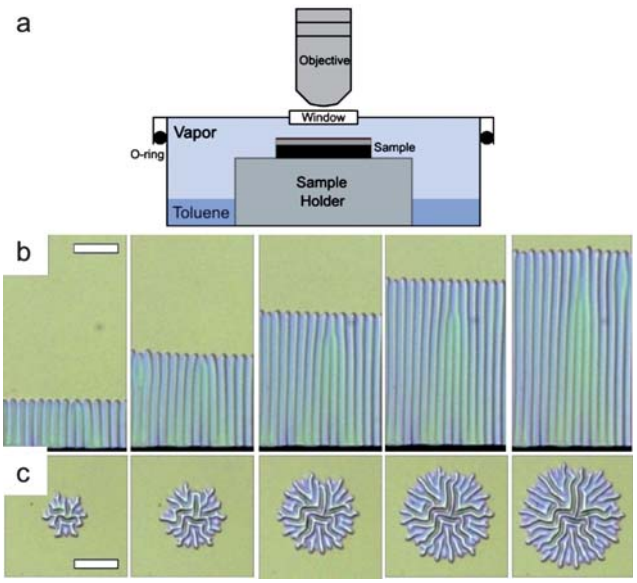

Fig. 1 (a) A schematic representation of the experimental set-up. From left to right: Successive optical micrographs of (b) the growth of parallel and (c) radial wrinkled domains, obtained after immersion of a Ti/PS/SiO_x trilayer in toluene vapors. The scale bar corresponds to 20 μm.

[a]*Interfaces & Fluides Complexes, Université de Mons, Laboratoire & Fluides Complexes, CIRMAP, Université de Mons, 20, Place du Parc, B-7000 Mons, Belgium. E-mail: pascal.damman@umons.ac.be*
[b]*Laboratoire Matière et Système Complexes, Université Paris Diderot - Paris 7, 75205 Paris Cedex 13, France*
[c]*Disease Biophysics Group, School of Engineering and Applied Sciences, Harvard University, 29 Oxford Street, Pierce Hall 322a, Cambridge, MA, 02138, USA*
† This paper is part of a *Soft Matter* themed issue on The Physics of Buckling. Guest editor: Alfred Crosby.
‡ These authors contributed equally to this work

the multilayers in toluene vapors at room temperature in a homemade device, allowing *in situ* optical microscopy observations (Fig. 1a). Regular wrinkles spontaneously form and propagate together with the diffusion front (Fig. 1b). The resulting wrinkling patterns do not show the usual labyrinthine morphology[13,15] but are clearly determined by the geometry of the diffusion process. Parallel wrinkles (Fig. 1b) are observed when the solvent diffuses from the edge yielding a linear front. Radial organization of wrinkles (Fig. 1c) arises from point-like diffusion starting at tiny holes/defects randomly distributed in the thin metal layer. Interestingly, the wrinkled domains grow and meet together in such a way that they adjust their orientation to avoid the formation of "expensive" dislocations (Fig. 2). This phenomenon occurs until the whole surface is decorated with wrinkles. Finally a labyrinthine-like morphology made of large domains of straight parallel wrinkles emerges, the size of the domains being determined by the distances between the native individual patterns. This continuous re-organization illustrates the dynamics of the wrinkles observed for a purely elastic foundation.

A detailed description of both the mechanism at the origin of the wrinkling phenomenon and the particular orientation of the wrinkles can be found in Ref. 23.

For very long polymer chains ($M_w \sim 1.5$ MDa), the rheological behavior of the polymer layer is essentially elastic in spite of the diffusion of toluene. Indeed, the large number of entanglements per chain for these polymer films requires very long diffusion times (*i.e.*, related to the reptation time) to obtain a viscous fluid. For these samples, the characteristic wrinkle wavelength λ selected by the system can thus be determined by the balance between the bending energy of the metal film, which favors large λs, and the elastic deformation of the rubbery polymer layer, which in contrast favors small ones.[13,15,23,24] A similar approach is used to describe the wavelength in the case of thermal wrinkling with an elastic foundation.[13,15]

Hierarchical wrinkling

In contrast with the high M_w samples described in the previous section, polystyrene (PS) films made up of small chains rapidly become viscous during solvent diffusion (they remain, however, elastic for experimental times shorter than the Rouse or reptation times of the chains). Surprisingly, different wrinkled patterns are obtained by solvent diffusion in these low M_w polymer layers (2 kDa < M_w < 75 kDa). The formation of a hierarchical structure of folds is observed (Fig. 3). Due to the diffusion process, this pattern shifts forward as it grows, closely following the wavefront. For both linear and radial symmetry, a discrete evolution of the wavelength is observed along the direction perpendicular to the diffusion front. We observe a continuous growth of "juvenile" wrinkles with the same λ located at the diffusive front. With time (*i.e.*, staying at the same location!), these wrinkles spontaneously evolve toward "mature" wrinkles characterized by larger λs. Interestingly, the evolution of λ can be rationalized by a simple power law for all studied samples (Fig. 4b). All data closely follows $\lambda \propto y^{1/3}$, y being the distance from the diffusion front (Fig. 4a).

The mechanism leading to the growth of these new hierarchical structures of folds in a compressed rigid membrane should involve bending of the sheet, viscous flow in the polymer layer and solvent diffusion. To get a first insight into this complex mechanism, we will consider a simplified system involving only bending and viscous flow: the evolution of homogeneous wrinkled patterns obtained during thermal compression of Ti/PS/SiO_x trilayers. In fact, increasing the solvent fraction in a polymer film produces a similar effect to a thermal jump. Indeed, adding solvent to a glassy polymer reduces its glass transition temperature, T_g, that can decrease well below the ambient temperature.[25] Similarly, heating the polymer above its glass transition temperature induces the transition from the glassy to the rubbery state. Fig. 5 shows the evolution of wrinkled patterns when heated above T_g. For such a viscoelastic fluid, the pattern wavelength is driven by elasticity at the very beginning of the wrinkling and is thus determined by the thicknesses and elastic moduli of the metal and polymer layer, such as: $\lambda_0 \sim (hH_p)^{1/2}(E/E_p)^{1/6}$ (where h, H_p and E, E_p are the metal and polymer thicknesses and moduli,

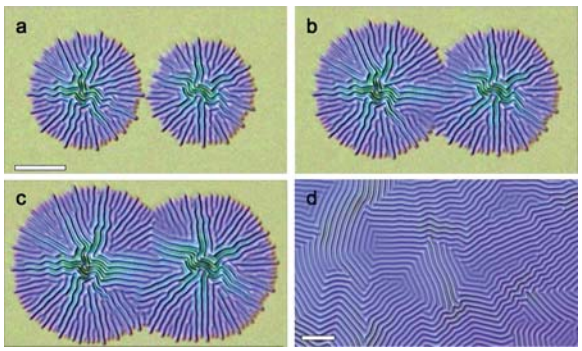

Fig. 2 (a)–(c) Successive optical micrographs of two radial wrinkled patterns joining together. (d) The final morphology arising from the meeting of several radial patterns. The scale bar corresponds to 20 μm.

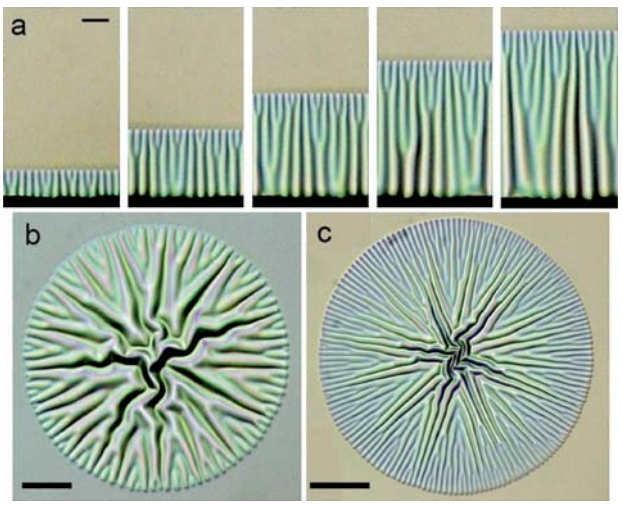

Fig. 3 (a) Successive optical micrographs of the growth of a wrinkled domain obtained after immersion in toluene vapors of a Ti/PS/SiO_x multilayer formed by a 15 nm thick titanium layer deposited on a 0.25 μm thick polystyrene layer ($M_w = 75$ kDa) on top of a silicon substrate. From left to right, after 10 s, 35 s, 60 s, 85 s, and 110 s immersion in toluene vapors (scale bar 10 μm). (b, c) Radial wrinkled patterns obtained with similar conditions ((b) 15 kDa, and (c) 75 kDa).

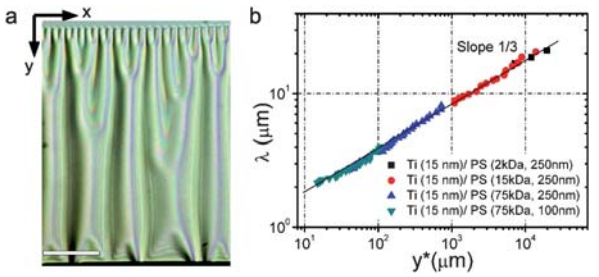

Fig. 4 (a) Optical micrograph of a wrinkled domain obtained after immersion in toluene vapors of a Ti/PS/SiO_x multilayer formed by a 15 nm thick titanium layer deposited on a 0.25 μm thick polystyrene layer ($M_w = 15$ kDa) on top of a silicon substrate. (b) Evolution of the wavelength *versus* the distance from the diffusion front for different low molecular weight polymers.

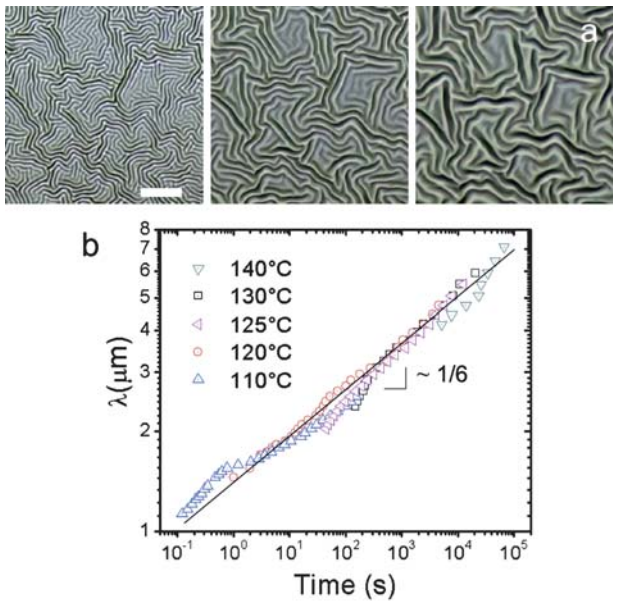

Fig. 5 (a) Thermal wrinkling. Optical micrographs of the temporal evolution of wrinkled Ti(15 nm)/PS(250 nm; 15 kDa)/SiO_x trilayers after 1, 2 and 30 min at 130 °C, from left to right, respectively. The scale bar corresponds to 20 μm. (b) Evolution of the wavelength *versus* time of wrinkled Ti(15 nm)/PS(250 nm; 15 kDa)/SiO_x at different temperatures. Curves were shifted thanks to the time–temperature principle (Williams-Landel-Ferry (WLF) equation).

respectively).[13,15] This elastic regime lasts until the polymer chains relax (*via* either Rouse or reptation dynamics), which marks the transition between elastic and viscous regimes. Beyond the relaxation time, we found that the wrinkle wavelength increases continuously with time and follows a power law with an exponent close to 1/6 (Fig. 5b).

The dynamics of these wrinkled patterns can be rationalized by considering the bending energy of the rigid membrane, that is minimized for infinite wavelength, and the energy dissipated within the polymer flow. The bending energy U_b is proportional to the square of the local membrane curvature: $U_b \sim \int Eh^3C^2 dx$. For a sinusoidal profile of wavelength λ and amplitude A, the typical local curvature is $C \sim A/\lambda^2 \sim \sqrt{\delta}/\lambda$ (by considering inextensibility, the compression strain, δ is given by A^2/λ^2). The bending energy U_b becomes therefore:

$$U_b \sim Eh^3 \frac{A^2}{\lambda^3} \sim Eh^3 \frac{\delta}{\lambda} \quad (1)$$

Because U_b is a decreasing function of λ, once the polymer is able to flow, the membrane deforms to achieve larger wavelengths (the wrinkle amplitude also increases since inextensibility yields $A \sim \lambda\sqrt{\delta}$). When the wavelength and the amplitude change, incompressibility of PS implies a flow within the polymer layer, the maximum horizontal velocity being given by $v = du/dt \sim (1/H_p)\, d(A\lambda)/dt$, considering the condition of incompressibility $uH_p \sim A\lambda$. Assuming a no slip boundary condition at the membrane and substrate interfaces, the velocity gradient related to the shear flow should be given by $\partial v/\partial z \sim v/H_p$. The power dissipated by this shear flow, integrated over the polymer thickness, is finally given by

$$P_{visc} \sim \int_0^{\lambda}\int_0^{H_p} \eta(\partial v/\partial z)^2 dx dz \sim \frac{\eta}{H_p^3}\lambda^3\dot{\lambda}^2\delta \quad (2)$$

where η is the polymer viscosity.

The variation of the membrane elastic energy with time should be equal to the dissipated power: $dU_b/dt = -P_{visc}$. Hence, the wavelength obeys the following ordinary differential equation,

$$\frac{\eta}{H_p^3}\delta\lambda^3\dot{\lambda}^2 \sim Eh^3\frac{\delta}{\lambda^2}\dot{\lambda} \quad (3)$$

Solving this differential equation yields the time evolution of the wavelength given by the relation,

$$\lambda \sim (hH_p)^{1/2}(E/\eta)^{1/6}t^{1/6} \quad (4)$$

The evolution of the wavelength with time given in Fig. 5 is in very good agreement with this scaling law over 6 orders of magnitude. The master curve was obtained by shifting the "rough" data recorded at various temperatures with a_T parameters computed from the WLF relation of PS.[26]

The balance between bending energy and viscous dissipation is well understood. Now, we go back to the formation of the hierarchical patterns observed for wrinkling of low M_w polymer from solvent diffusion (Fig. 3). As seen in Fig. 4a, the wavelength evolves from the diffusion front to the sample edge (or the point-like defect for radial patterns). In fact, as the diffusion domain expands, the polymer at the front has just become soft enough to allow wrinkling. The wavelength of these "juvenile" wrinkles, λ_0, is thus determined by elasticity and is very small (close to 1 μm). As one goes towards the edge of the sample, the polymer has been plastified for a longer period of time and is characterized by a purely viscous behaviour. These "mature" wrinkles exhibit larger wavelengths (larger than 10 μm). Combining roughly the dynamics of wrinkles on a viscous foundation $\lambda \sim t^{1/6}$ (see eqn (4)) with the diffusion process which should scale as $y \sim t^{1/2}$, y being the distance from the diffusion front, we could easily find that $\lambda \sim y^{1/3}$, which is in agreement with the experiments, as shown in Fig. 4b.

Furthermore, the above interpretation is also consistent with the observation that the evolution of the wavelength (and amplitude) is sharper for very low M_ws, considering the drastic

evolution of polymer viscosity with M_w[25]. According to eqn (4), the wavelength should increase faster with time for low viscosity polymers (low M_w), which implies steeper spatial variations. The rheological properties of the polymer and the geometry of the diffusion front thus play a crucial role in the formation of complex wrinkled patterns. By modifying the M_w of PS, for instance, we can shift from homogeneous to hierarchical wrinkled patterns. It should be noted however that the dynamics of these patterns can also be affected by the localized defects required to double the wavelength (*i.e.*, these defects exhibit a finite Gaussian curvature leading to high energetic penalties). The exact role of these defects is currently investigated.

As shown in Fig. 3, these complex patterns exhibit a gradient in amplitude and wavelength which increases from the periphery to the center. The diffusion controlled wrinkling process thus provides a unique tool to create patterns with well-controlled gradually changing topographies.

In the last part of the paper, we will show that wrinkling can be consider as a valuable tool for the design and fabrication of structured surfaces suitable for applications in the field of biotechnology.

Cell mechanosensitivity

One of the promising applications of hierarchical wrinkled patterns concerns the development of substrates to stimulate and commit cell functions such as adhesion, motility or proliferation through topographical interactions.[27] To date, research efforts have been largely focused on examining how anisotropic structures such as ridges or grooves influence cell responses, irrespective of the length scale (nano- or microscale). As a consequence, the variety of studied structured surfaces with different shapes and sizes may account for the discrepancies between reported observations on the mechanism of lamellipodia and filopodia formation in response to topography.[28] Therefore, the design of substrates with variable topographic features while maintaining constant physical (*e.g.* rigidity) and chemical (*e.g.* surface tension) properties to avoid undesirable responses is a significant challenge.

By replicating the original wrinkled patterns presented in the first part of this paper, we fabricated optically transparent structured substrates (see the Experimental section) to illustrate the relevance of our structuration method by studying the mechanosensitivity in response to local variations in topography, based on (i) cell-substrate adhesion and (ii) cell sensing mechanisms.

Cell adhesion. Cells adhere to the extracellular matrix (ECM) *via* integrin-mediated adhesions that link the ECM to the actin cytoskeleton. In addition to their function as adhesion sites, focal adhesions are also the sites at which forces are transmitted to the substrate.[29,30] Therefore the spatial distribution of focal adhesion sites should play a major role in the regulation of cell adhesion and cytoskeletal organization. With this in mind, we explored the possibility to control the distribution of sites of cell adhesion to the substrate by using wrinkled patterns. This was achieved by mapping the correlation between the localization of adhesion sites and topographic features.

The distribution of focal adhesions under fibroblasts onto flat and wrinkled PDMS domains was detected by microscopy with fluorescence labelling of specific adhesion molecules. Immunohistochemical staining of vinculin, which is one of the most prominent cytoskeletal proteins in focal adhesion, indicates the localization of specific binding sites between cells and substrates. On flat domains, fibroblasts make numerous vinculin-positive focal contacts, which are exclusively distributed along the cell perimeter of leading and trailing edges (Fig. 6a, white arrowheads). In contrast, the distribution of focal contacts was drastically modified for cells with leading and trailing edges in contact with structured domains. Indeed, vinculin staining clearly reveals the presence of focal adhesions within the central area of cell protrusions on structured domains (Fig. 6b, white arrowheads). The overlay of the thresholded vinculin staining with the topography (Fig. 6c and d) helps in demonstrating the spatial correlation of focal adhesion sites with the topographic features. Our results show that integrin binding is preferentially located on the top of ridges located at the center of the pattern, corresponding to microscale topographic features (from 950 to 725 nm groove depth). This observation indicates that fibroblasts cannot bridge the gap of microscale structured zones and thus lead to the confinement of cell attachment on the top of the rounded microscale wrinkles. In contrast, no effect of nanoscale features on the spatial distribution of focal contacts has been

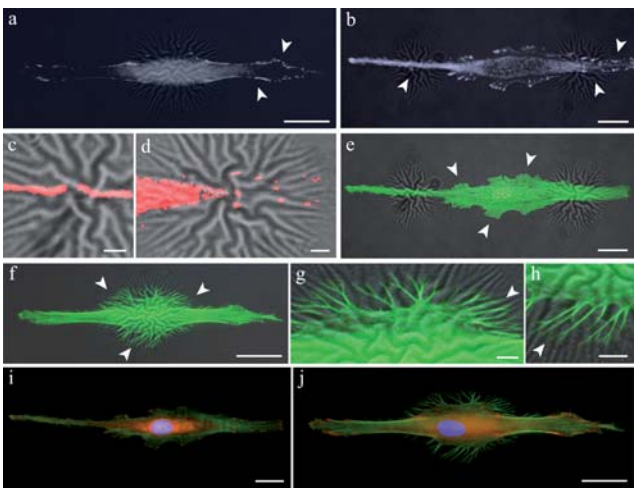

Fig. 6 Immunofluorescence images of fibroblast cells cultured on textured PDMS surfaces with a localized topographical gradient. Images (a) and (b) present the vinculin distribution of leading and trailing edges in contact with (a) a flat surface and (b) a hierarchical wrinkled pattern, respectively. White arrowheads show that (a) fibroblasts exhibit discrete focal contacts located at the cell periphery on flat substrates and (b) that integrin binding is limited to the top of the ridge when cells bridge microscale patterns. Images (c) and (d) present a close-up of the vinculin distribution (in red) on microscale wrinkles obtained from (b) after processing. Images (e), (f), (g) and (h) show the organization of filamentous actin in green. Extension of cellular protrusions from the cell body: (e) large lamellipodial extensions on flat surfaces and (f) multiple filopodial structures on structured surfaces. Images (g) and (h) show a close-up of the alignment of filopodia with nanoscale features. Images (i) and (j) are merged images of F-actin (green), vinculin (red) and nuclei (blue). The scale bars correspond to 20 μm for images (a), (b), (e), (f), (i), (j) and 5 μm for images (c), (d), (g) and (h).

observed, suggesting that integrin-binding sites are preferentially sensitive to micrometre-range features.

Cell sensing mechanisms. Two alternate forms of actin machinery coexist in most motile cells: lamellipodia which seem designed for persistent protrusion over a surface, and filopodia which appear to perform sensory and exploratory functions to steer cells depending on cues from the environment.[31] Therefore, understanding how a cell type expresses the lamellipodial or filopodial form of the actin machinery in response to topography is essential for understanding cell sensing mechanisms as well as for applications in the field of biotechnology. To determine how a cell chooses among these alternative modes of cellular protrusions in response to a specific topographic scale (nano *vs.* macro), we observed the behavior of fibroblasts plated on flat and wrinkled domains with well-controlled gradually changing topographies.

Lamellipodia and filopodia protrusions are driven by dynamic local actin polymerization and can thus be probed *via* actin fluorescence labeling. Fig. 6e shows that fibroblasts on flat surfaces extend a few large lamellipodial extensions from the cell-body. On the contrary, fibroblasts with their cell body deposited on a wrinkled domain were found to extend numerous filopodial structures (Fig. 6f). These observations suggest a specific response of fibroblast cells to the topographical modifications of their surrounding matrix by extending filopodia, that is in agreement with a sensory role of filopodia protusions. As shown in Fig. 6g–h, we have noticed that filopodia are preferentially aligned along nanoscale features (from 60 to 140 nm groove depth) located at the periphery of the pattern. Whereas micrometric wrinkles located at the center of the pattern are involved in filopodia attachment, as shown by discrete vinculin spots (see Fig. 6d, 850 nm groove depth). Although previous works suggest that filopodia can feel variations of surface topography, many contradictory results on the alignment of filopodia have been reported.[32] In light of this, our observations suggest that alignment of filopodia may be preferentially driven by nanoscale topographic features, whereas microscale patterns are necessary to permit filopodia attachment.

Although already particularly interesting, a systematic study is needed to quantify these preliminary results.

Conclusions

We have reported on a novel lithography-free method for obtaining sophisticated patterns with a gradient of topography ranging from the nano- to the microscale. We have demonstrated that solvent-induced wrinkling of multilayer systems can lead to the formation of a hierarchical structure of folds. We have showed the crucial role of the rheological properties of the polymer and the geometry of the diffusion front in the formation of the wrinkled patterns obtained. In an attempt to exploit the topography of these patterns, we have considered hierarchical wrinkled patterns as a valuable tool to modulate cell mechanosensitivity. We believe that the present structuration method will open up new directions to achieve a desired optical effect, to prepare controlled substrates for bacterial organization, to develop sophisticated microfluidic devices or to promote cell mechanosensing for tissue engineering.

Experimental section

Fabrication of the multilayers

The multilayers were prepared in two steps: (i) spin coating atactic polystyrene (PS) solutions in toluene on bare silicon substrates to produce films with thicknesses around 0.25 μm. Polymers with molecular weights ranging from 10^3 to 10^6 Da were used, (ii) deposition of a 15 nm thick titanium (Ti) layer onto the polymer surface by thermal evaporation.

Buckling process

Wrinkling was induced by immersing the multilayers in toluene vapor at room temperature in a homemade device allowing *in situ* optical microscopy observations. Toluene is a good solvent for PS that can swell the polymer layer by diffusion through the Ti membrane.

PDMS replica molding

PDMS replicas were prepared by spin-coating a 10 : 1 (w/w) degassed mixture of PDMS prepolymer and curing agent (Sylgard 184, Dow Corning) on 25 mm diameter clean glass coverslips. The Ti layer was passivated with a fluorosilane (tridecafluoro-1,1,2,2-tetrahydrooctyl-1-trichlorosilane, Gelest) for 30 min in a vacuum to facilitate the removal of the PDMS from the structured surface.[33] PDMS coated coverslips were cast against the structured Ti layers and the elastomer was cured overnight at 65 °C. After curing, the PDMS coated coverslips were gently peeled off the titanium substrate. The PDMS replicas were washed with ethanol and then made hydrophilic by exposure to ultraviolet ozone (UV/O_3) activation for 15 min. Cells do not readily adhere to PDMS, thus activated PDMS replicas were finally coated with a sterile aqueous fibronectin (FN) solution for 1 h at room temperature to promote cell attachment.

Cell culture

Normal Human Dermal Fibroblasts (NHDFs, American Type Culture Collection) were cultured in Dubelcco's Modified Eagle Medium (DMEM) supplemented with 10% Fetal Bovine Serum (FBS) and penicillin/streptomycin (100 U/mL, Invitrogen). The cells were kept at 37 °C and 5% CO_2. At confluence, NHDFs were detached from the culture dishes using trypsin/EDTA followed by centrifugation (2000 rpm, 5 min). NHDFs were re-suspended in fresh culture medium and seeded at the density of 50.10^3 cells mL^{-1} on FN-coated structured PDMS coverslips.

Immunocytochemisry

Components of the cytoskeleton were made visible using fluorescent staining techniques. Staining of fibroblasts for actin and vinculin followed established protocols.[34] Briefly, fibroblasts, cultured on structured substrata, were rinsed 3 times with PBS (pH = 7.2), fixed in a fresh 4% paraformaldehyde solution for 15 min and permeabilized with 1% Triton X-100 for 10 min. Coverslips were rinsed extensively with PBS and incubated with Alexa Fluor 488 phalloidin to stain filamentous actin (Molecular

Probes, Leiden, The Netherlands) for 45 min at 37 °C. Finally, vinculin was stained with mouse polyclonal primary antibodies followed by labelling with goat anti-rabbit secondary antibodies IgG (Molecular Probes, Leiden, The Netherlands) for 45 min at 37 °C. The distribution of actin and vinculin was observed by fluorescence microscopy and correlated with the surface topography. For each cell, three separate images were taken; one for each of the two fluorescence filter sets utilized and one additional differential interference contrast (DIC) image showing the underlying surface topography. When combined, the staining could be overlaid on the topography, unambiguously demonstrating the interaction of stained intracellular components with the underlying topographic features. Digital images were captured with a QuantEM 512SC deep-cooled CCD camera (Photometrics, Tuscon, AZ) mounted on a Nikon TI inverted confocal microscope equipped with 40×, 60× and 100× oil immersion objectives.

Image processing

The position and the dimension of the focal contacts were quantified to investigate their relationships to the topographic features. These were observed after image processing using ImageJ software. In detail, original images of immunostained cells were thresholded, based on the mean and standard deviation of the gray level distribution of all pixels, respectively. After obtaining a binary image, the segmented images were converted to a binary mask such that all pixels above the threshold were assigned a value of one and all those below were assigned a value of zero. The background and sub-threshold regions are color-coded black and red, respectively, in the final images.

Acknowledgements

The authors thank Prof. Alexandra Belayew (Université de Mons, Belgium) for providing cell culture support and Marie Versaevel for her technical assistance in cell culture. S.G. gratefully acknowledges Prof. Pierre Bongrand (Université de la Mediterranée, Marseille, France) for kindly providing the NHDF cell line. This work was supported by the National Fund for Scientific Research (F.R.S.-FNRS) (Mandat d'Impulsion Scientifique), the Walloon Region (REMANOS project) and by an ESF - Eurocores project EBioAdI (FANAS). S.G. is Chargé de Recherches du F.R.S.-FNRS. K.K.P. acknowledges the financial support of NIH R01HL079126-01A2.

References

1 D. K. Khang, H. Jiang, Y. Huang and J. A. Rogers, *Science*, 2006, **311**, 208.
2 E. P. Chan, E. Smith, R. Hayward and A. J. Crosby, *Adv. Mater.*, 2008, **20**, 711.
3 B. Kolaric, K. Branko, H. Vandeparre, S. Desprez, R. A. L. Vallée and P. Damman, *Appl. Phys. Lett.*, 2010, **96**, 043119.
4 W. H. Koo, S. M. Jeong, F. Araoka, K. Ishikawa, S. Nishimura, T. Toyooka and H. Takezoe, *Nat. Photonics*, 2010, **4**, 222.
5 P. C. Lin and S. Yang, *Soft Matter*, 2009, **5**, 1011.
6 R. Langer and D. A. Tirrell, *Nature*, 2004, **428**, 487.
7 M. Goldberg, R. Langer and X. Q. Jia, *J. Biomater. Sci., Polym. Ed.*, 2007, **18**, 241.
8 D. K. Yi, M. J. Kim, L. Turner, K. S. Breuer and D. Y. Kim, *Biotechnol. Lett.*, 2006, **28**, 169.
9 M. J. Dalby, M. O. Riehle, H. J. Johnstone, S. Affrosman and A. S. Curtis, *Tissue Eng.*, 2002, **8**, 1099.
10 S. Patel, K. Kurpinski, R. Quigley, H. Gao, B. S. Hsiao, M. M. Poo and S. Li, *Nano Lett.*, 2007, **7**, 2122.
11 E. K. Yim, R. M. Reano, S. W. Pang, A. F. Yee, C. S. Chen and K. W. Leong, *Biomaterials*, 2005, **26**, 5405.
12 K. Lee, S. Park, C. Mirkin, J. Smith and M. Mrksich, *Science*, 2002, **295**, 1702.
13 N. Bowden, S. Britain, A. G. Evans, J. W. Hutchinson and G. M. Whitesides, *Nature*, 1998, **393**, 146.
14 J. Genzer and J. Groenewold, *Soft Matter*, 2006, **2**, 310.
15 H. Vandeparre, J. Leopoldes, C. Poulard, S. Desprez, G. Derue, C. Gay and P. Damman, *Phys. Rev. Lett.*, 2007, **99**, 188302.
16 N. Bowden, W. T. S. Huck, K. E. Paul and G. M. Whitesides, *Appl. Phys. Lett.*, 1999, **75**, 2557.
17 T. Ohzono, S. I. Matsushita and M. Shimomura, *Soft Matter*, 2005, **1**, 227.
18 T. Okayasu, H. L. Zhang, D. G. Bucknall and G. A. D. Briggs, *Adv. Funct. Mater.*, 2004, **14**, 1081.
19 W. T. S. Huck, N. Bowden, P. Onck, T. Pardoen, J. W. Hutchinson and G. M. Whitesides, *Langmuir*, 2000, **16**, 3497.
20 S. J. Kwon, P. J. Yoo and H. H. Lee, *Appl. Phys. Lett.*, 2004, **84**, 4487.
21 P. J. Yoo, K. Y. Suh, S. Y. Park and H. H. Lee, *Adv. Mater.*, 2002, **14**, 1383.
22 P. J. Yoo and H. H. Lee, *Phys. Rev. Lett.*, 2003, **91**, 154502.
23 H. Vandeparre and P. Damman, *Phys. Rev. Lett.*, 2008, **101**, 124301.
24 E. Cerda and L. Mahadevan, *Phys. Rev. Lett.*, 2003, **90**, 074302.
25 M. Rubinstein and R. H. Colby, *Polymer Physics*, Oxford University Press, 2003.
26 P. Damman, S. Gabriele, S. Coppée, S. Desprez, D. Villers, T. Vilmin, E. Raphaël, M. Hamieh, S. Al Akhrass and G. Reiter, *Phys. Rev. Lett.*, 2007, **99**, 036101.
27 A. Schweikart and A. Fery, *Microchim. Acta*, 2009, **165**, 249.
28 S. Fujita, M. Ohshima and H. Iwata, *J. R. Soc. Interface*, 2009, **6**, S269.
29 N. Q. Balaban, U. S. Schwarz, D. Riveline, P. Goichberg, G. Tzur, I. Sabanay, D. Mahalu, S. Safran, A. Bershadsky, L. Addadi and B. Geiger, *Nat. Cell Biol.*, 2001, **3**, 466.
30 K. K. Parker, A. L. Brock, C. Brangwynne, R. J. Mannix, N. Wang, E. Ostuni, N. A. Geisse, J. C. Adams, G. M. Whitesides and D. E. Ingber, *FASEB J.*, 2002, **16**, 1195.
31 M. R. Mejillano, S.-i. Kojima, D. A. Applewhite, F. B. Gertler, T. M. Svitkina and G. G. Borisy, *Cell*, 2004, **118**, 363.
32 A. I. Teixeira, G. A. McKie, J. D. Foley, P. J. Bertics, P. F. Nealey and C. J. Murphy, *Biomaterials*, 2006, **27**, 3945.
33 S. Gabriele, A. M. Benoliel, P. Bongrand and O. Theodoly, *Biophys. J.*, 2009, **96**, 4308.
34 M. A. Bray, S. P. Sheehy and K. K. Parker, *Cell Motil. Cytoskeleton*, 2008, **65**, 641.

